Research Article

Hui-Shen Shen*, Yin Fan*, and Yeqing Wang

Tension buckling and postbuckling of nanocomposite laminated plates with in-plane negative Poisson's ratio

https://doi.org/10.1515/ntrev-2023-0173
received September 7, 2023; accepted November 28, 2023

Abstract: Mechanical metamaterials with negative Poisson's ratio (NPR) have emerged as a novel class of engineering material, and have attracted increasing attention in various engineering sectors. Most studies available on the buckling problem of laminated plates with positive or NPR are those under uniaxial compression. Here, we report that the buckling phenomenon may occur for auxetic nanocomposite laminated plates under uniaxial tension when the unloaded edges of the plates are immovable. Two types of nanocomposites are considered, including graphene/Cu and carbon nanotube/Cu composites. Governing equations of the auxetic nanocomposite laminated plates are formulated based on the framework of Reddy's higher-order shear deformation theory. In modeling, the von Kármán nonlinear strain–displacement relationship, temperature-dependent material properties, thermal effects, and the plate–substrate interaction are considered. The explicit analytical solutions for postbuckling of auxetic nanocomposite laminated plates subjected to uniaxial tension are obtained for the first time by employing a two-step perturbation approach. Numerical investigations are performed for tension buckling and postbuckling behaviors of auxetic nanocomposite laminated rectangular plates with in-plane NPR rested on an elastic substrate under temperature environments.

Keywords: nanocomposites, auxetic laminates, tension buckling, rectangular plate, elastic substrate, temperature-dependent

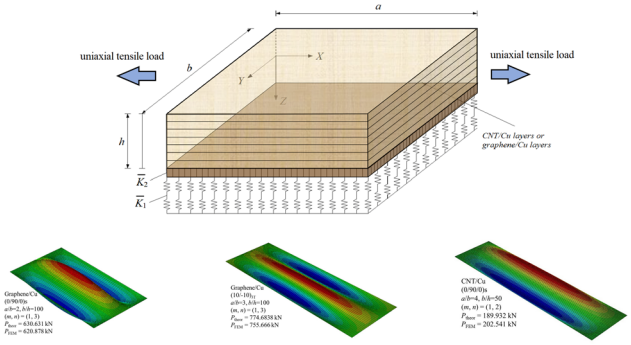

Graphical abstract

1 Introduction

Buckling is an important problem for the thin plates subjected to uniaxial or biaxial compression [1]. Under tensile loads, thin plates usually do not experience buckling. However, according to the literature survey, there are two special cases, in which buckling can occur under tensile loads, namely "tension buckling," for the thin plates/sheets. One case is if a plate contains a hole [2–4] or a crack [5–7], the compressive stresses arise locally near the hole or the crack under a uniaxial tensile load, where these compressive stresses may cause local buckling. Another case is wrinkling (*i.e.*, local short-wavelength buckling), which is commonly observed in stretched-thin sheets [8–12] and single-layer graphene sheets [13–16] due to the variation of Poisson's effect. For nanocomposite structures, which are generally considered as the next-generation composite structures, although much research has been done on the buckling and postbuckling analyses of nanocomposite plates under uniaxial or biaxial compression, no attention is paid to the buckling of nanocomposite plates when they are subjected to a tensile load. The buckling of nanocomposite plates under tensile load represents a unique and crucial failure mode in the design of these structures, which has not been reported in the literature. To guide the design and optimization of nanocomposites for future engineering applications, it is of great significance to establish a scientific and theoretical tool to

* **Corresponding author: Hui-Shen Shen**, School of Aeronautics and Astronautics, Shanghai Jiao Tong University, Shanghai 200240, China, e-mail: hsshen@sjtu.edu.cn
* **Corresponding author: Yin Fan**, School of Aeronautics and Astronautics, Shanghai Jiao Tong University, Shanghai 200240, China, e-mail: yfan1987@sjtu.edu.cn
Yeqing Wang: Department of Mechanical and Aerospace Engineering, Syracuse University, Syracuse, NY 13244, United States of America

predict the critical tension buckling load, and hence, the factor of safety under this unique buckling failure mode.

Auxetic laminated composites with negative Poisson's ratio (NPR) are one class of mechanical metamaterials. With the development of nanotechnology and additive manufacturing technology [17,18], nanofillers such as graphene sheets [19] or carbon nanotubes (CNTs) [20] can be embedded in a single-crystal copper matrix to achieve auxetic nanocomposite laminates [21,22]. Owing to their special properties and characteristics, auxetic nanocomposite materials have shown better performance in certain aspects than those of conventional materials and are expected to have a wide range of technological applications [23,24].

Recently, Shen *et al.* [25] combined the functionally graded (FG) concept with the auxetic concept to design the FG-GRMMC (graphene-reinforced metal-matrix composite) laminates. Considering the auxetic effect of GRMMCs, Shen and his co-authors [25,26] investigated the impact of in-plane NPR on the compressive postbuckling behaviors of FG-GRMMC laminated and sandwich plates subjected to uniaxial compression. Unlike fiber-reinforced composite (FRC), graphene-reinforced composite (GRC) and carbon nanotube-reinforced composite (CNTRC) laminated plates with positive Poisson's ratios [27–29] where the buckling loads and initial postbuckling load–deflection curves for the plate with unloaded edges that are movable (*i.e.*, displacement is unconstrained in the in-plane direction) are higher than those of the same plate with unloaded edges that are immovable (*i.e.*, displacement is constrained in the direction perpendicular to the loaded edges), the auxetic GRMMC laminated plates showed the opposite behavior. Specifically, for auxetic laminated plates, the buckling loads and postbuckling load–deflection curves with unloaded edges that are movable in the in-plane direction are lower than those of the same plate under immovable unloaded edges. This indicates that the unique lateral contraction of the auxetic laminates under uniaxial compressive load locally enhanced the buckling strength. Such an exceptional behavior leads us to believe that auxetic laminated plates with unloaded edges that are immovable may buckle under a uniaxial tensile load as compressive reaction force will be produced on unloaded edges to restrict the lateral expansion of the auxetic plates under uniaxial tension. This provides the motivation for the present investigation.

The present research is to investigate the buckling and postbuckling behavior of auxetic nanocomposite laminated plates with unloaded edges that are immovable and subjected to the uniaxial tensile load under thermal environmental conditions. In the current study, we chose two types of auxetic nanocomposite laminates. One is a graphene/Cu laminated plate with in-plane NPR and the other is a CNT/Cu laminated plate with in-plane NPR. The material properties of both graphene/Cu and CNT/Cu composites are temperature-dependent. The governing equations of the auxetic nanocomposite laminated plates are established based on the framework of Reddy's higher-order shear deformation theory (HSDT). In modeling, the von Kármán nonlinear strain–displacement relationship, the effect of temperature, the interaction between the plate and substrate, and the effect of the plate's initial geometric imperfection are also taken into consideration. The explicit analytical solutions for buckling and postbuckling of auxetic nanocomposite laminated plates subjected to uniaxial tension are obtained for the first time by employing a two-step perturbation approach. The impacts of the plate aspect ratio, the plate width-to-thickness ratio, temperature variation, and foundation stiffness on tension buckling and postbuckling behavior of auxetic nanocomposite laminated plates are discussed in the numerical investigation.

2 Modeling

Consider an N-ply laminated rectangular plate, where each ply is made of nanocomposites having an in-plane NPR. As shown in Figure 1, a is the length, b is the width, and h is

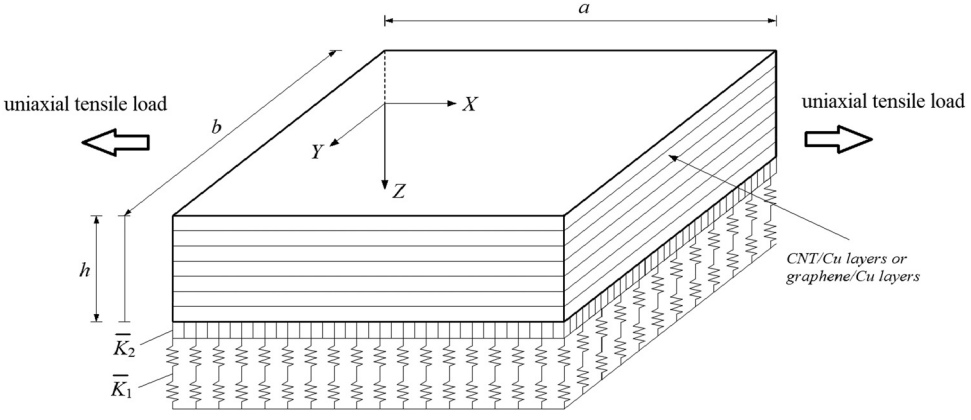

Figure 1: Auxetic nanocomposite laminated rectangular plate rests on an elastic substrate under uniaxial tensile load.

the total thickness of the plate. The coordinate system (X, Y, Z) is located on the middle surface of the plate with its origin placed at one corner of the plate, where the X and Y axes are set along the length and the width directions, respectively, while the Z-axis is set along the thickness direction pointing downward. The plate is rested on an elastic substrate that is idealized as a Pasternak-type foundation model with two stiffnesses, where $\bar{K}_1$ denotes the vertical spring stiffness and $\bar{K}_2$ denotes the shearing layer stiffness.

The plate is exposed to elevated temperature and is subjected to uniaxial tensile load. Based on the framework of HSDT of Reddy [30] and that coupled with the von Kármán nonlinear strain–displacement relationships, the governing equations for the postbuckling of the nanocomposite laminated plate with in-plane NPR are given by Shen [1]

$$\tilde{L}_{11}(\bar{W}) - \tilde{L}_{12}(\bar{\Psi}_x) - \tilde{L}_{13}(\bar{\Psi}_y) + \tilde{L}_{14}(\bar{F}) - \tilde{L}_{15}(\bar{N}^T) - \tilde{L}_{16}(\bar{M}^T) + \bar{K}_1\bar{W} - \bar{K}_2\nabla^2\bar{W} = \tilde{L}(\bar{W} + \bar{W}^*, \bar{F}), \tag{1a}$$

$$\tilde{L}_{21}(\bar{F}) + \tilde{L}_{22}(\bar{\Psi}_x) + \tilde{L}_{23}(\bar{\Psi}_y) - \tilde{L}_{24}(\bar{W}) - \tilde{L}_{25}(\bar{N}^T) = -\frac{1}{2}\tilde{L}(\bar{W} + 2\bar{W}^*, \bar{W}), \tag{1b}$$

$$\tilde{L}_{31}(\bar{W}) + \tilde{L}_{32}(\bar{\Psi}_x) + \tilde{L}_{33}(\bar{\Psi}_y) + \tilde{L}_{34}(\bar{F}) - \tilde{L}_{35}(\bar{N}^T) - \tilde{L}_{36}(\bar{S}^T) = 0, \tag{1c}$$

$$\tilde{L}_{41}(\bar{W}) + \tilde{L}_{42}(\bar{\Psi}_x) + \tilde{L}_{43}(\bar{\Psi}_y) + \tilde{L}_{44}(\bar{F}) - \tilde{L}_{45}(\bar{N}^T) - \tilde{L}_{46}(\bar{S}^T) = 0, \tag{1d}$$

where $\bar{W}$ is the plate displacement in the Z direction, $\bar{W}^*$ is the initial geometric imperfection, $\bar{F}$ is the stress function defined by $\bar{N}_x = \partial^2\bar{F}/\partial Y^2$, $\bar{N}_y = \partial^2\bar{F}/\partial X^2$, and $\bar{N}_{xy} = -\partial^2\bar{F}/\partial X\partial Y$, and $\bar{\Psi}_x$ and $\bar{\Psi}_y$ are two rotations with respect to the Y and X axes. $\tilde{L}_{ij}(\,)$ represent the linear operators [1], and $\tilde{L}(\,)$ representing the nonlinear operator involving geometric nonlinearity in the von Kármán sense is expressed by

$$\tilde{L}(\,) = \frac{\partial^2(\,)}{\partial Y^2}\frac{\partial^2(\,)}{\partial X^2} - 2\frac{\partial^2(\,)}{\partial X\partial Y}\frac{\partial^2(\,)}{\partial Y\partial X} + \frac{\partial^2(\,)}{\partial X^2}\frac{\partial^2(\,)}{\partial Y^2}. \tag{2}$$

Meanwhile, the interaction of the plate foundation defined by $\bar{K}_1\bar{W} - \bar{K}_2\nabla^2\bar{W}$ along with the thermal effect is included in equations (1a)–(1d). The thermal forces, the thermal moments, and the higher-order thermal moments ($\bar{N}^T$, $\bar{M}^T$, $\bar{P}^T$) due to elevated temperature are given by

$$\begin{bmatrix} \bar{N}_x^T & \bar{M}_x^T & \bar{P}_x^T \\ \bar{N}_y^T & \bar{M}_y^T & \bar{P}_y^T \\ \bar{N}_{xy}^T & \bar{M}_{xy}^T & \bar{P}_{xy}^T \end{bmatrix} = \sum_{k=1}^{h_k}\int_{h_{k-1}} \begin{bmatrix} A_x \\ A_y \\ A_{xy} \end{bmatrix}_k (1, Z, Z^3)\Delta T \, \mathrm{d}Z, \tag{3a}$$

and $\bar{S}^T$ in equations (1c) and (1d) are given by

$$\begin{bmatrix} \bar{S}_x^T \\ \bar{S}_y^T \\ \bar{S}_{xy}^T \end{bmatrix} = \begin{bmatrix} \bar{M}_x^T \\ \bar{M}_y^T \\ \bar{M}_{xy}^T \end{bmatrix} - \frac{4}{3h^2}\begin{bmatrix} \bar{P}_x^T \\ \bar{P}_y^T \\ \bar{P}_{xy}^T \end{bmatrix}, \tag{3b}$$

In equation (3a), $\Delta T = T - T_0$ denotes the temperature increase with reference to temperature T_0, and

$$\begin{bmatrix} A_x \\ A_y \\ A_{xy} \end{bmatrix} = -\begin{bmatrix} \bar{Q}_{11} & \bar{Q}_{12} & \bar{Q}_{16} \\ \bar{Q}_{12} & \bar{Q}_{22} & \bar{Q}_{26} \\ \bar{Q}_{16} & \bar{Q}_{26} & \bar{Q}_{66} \end{bmatrix}\begin{bmatrix} c^2 & s^2 \\ s^2 & c^2 \\ 2cs & -2cs \end{bmatrix}\begin{bmatrix} \alpha_{11} \\ \alpha_{22} \end{bmatrix}, \tag{4}$$

where α_{11} and α_{22} are the thermal expansion coefficients in the longitudinal and transverse directions of the kth ply, respectively, and $\bar{Q}_{ij}$ represent the transformed elastic constants, defined by

$$\begin{bmatrix} \bar{Q}_{11} \\ \bar{Q}_{12} \\ \bar{Q}_{22} \\ \bar{Q}_{16} \\ \bar{Q}_{26} \\ \bar{Q}_{66} \end{bmatrix} = \begin{bmatrix} c^4 & 2c^2s^2 & s^4 & 4c^2s^2 \\ c^2s^2 & c^4 + s^4 & c^2s^2 & -4c^2s^2 \\ s^4 & 2c^2s^2 & c^4 & 4c^2s^2 \\ c^3s & cs^3 - c^3s & -cs^3 & -2cs(c^2 - s^2) \\ cs^3 & c^3s - cs^3 & -c^3s & 2cs(c^2 - s^2) \\ c^2s^2 & -2c^2s^2 & c^2s^2 & (c^2 - s^2)^2 \end{bmatrix}\begin{bmatrix} Q_{11} \\ Q_{12} \\ Q_{22} \\ Q_{66} \end{bmatrix}, \tag{5a}$$

$$\begin{bmatrix} \bar{Q}_{44} \\ \bar{Q}_{45} \\ \bar{Q}_{55} \end{bmatrix} = \begin{bmatrix} c^2 & s^2 \\ -cs & cs \\ s^2 & c^2 \end{bmatrix}\begin{bmatrix} Q_{44} \\ Q_{55} \end{bmatrix}, \tag{5b}$$

where

$$(Q_{11}, \ Q_{12}, \ Q_{22}) = \frac{1}{(1 - \nu_{12}\nu_{21})}(E_{11}, \ \nu_{21}E_{11}, \ E_{22}), \quad (Q_{44}, \ Q_{55}, Q_{66}) = (G_{23}, \ G_{13}, \ G_{12}), \tag{5c}$$

where E_{11}, E_{22}, G_{12}, G_{13}, G_{23}, ν_{12}, and ν_{21} are Young's moduli, shear moduli, and Poisson's ratios for the kth ply, and $c = \cos\theta$ and $s = \sin\theta$ (θ is the lamination angle with respect to the plate X-axis).

Besides the governing equations (1a)–(1d), for the boundary-value problem, we require the boundary conditions for the auxetic laminated plate. In order to derive the theoretical solution, the four edges of the auxetic laminated plate are assumed to be SSSS (*i.e.*, simply supported on all four edges). Specifically, on the $X = 0$ and $X = a$ edges,

$$\bar{W} = \bar{\Psi}_y = 0, \ \bar{M}_x = \bar{P}_x = 0, \tag{6a}$$

and on the $Y = 0$ and $Y = b$ edges,

$$\bar{W} = \bar{\Psi}_x = 0, \ \bar{M}_y = \bar{P}_y = 0, \tag{6b}$$

where $\bar{M}_x$ and $\bar{M}_y$ are the bending moments, and $\bar{P}_x$ and $\bar{P}_y$ are the higher-order moments, as given in the study of Reddy [30].

The tensile loads are applied on the $X = 0$ and $X = a$ edges and the two loaded edges are freely movable (*i.e.*, the displacement can move in the X-direction), while the other two unloaded edges are immovable (*i.e.*, the displacement is constrained in the Y-direction). The in-plane boundary condition on the $Y = 0$ and $Y = b$ edges is

$$\bar{V} = 0, \tag{7}$$

where $\bar{V}$ is the displacement of the plate in the Y direction, and equation (7) can be expressed in an average sense as

$$\int_0^a \int_0^b \frac{\partial \bar{V}}{\partial Y} \mathrm{d}Y \mathrm{d}X = 0, \tag{8a}$$

or

$$\begin{aligned} \int_0^a \int_0^b \Bigg\{ & \left[A_{22}^* \frac{\partial^2 \bar{F}}{\partial X^2} + A_{12}^* \frac{\partial^2 \bar{F}}{\partial Y^2} + \left(B_{26}^* - \frac{4}{3h^2} E_{26}^* \right) \left(\frac{\partial \bar{\Psi}_x}{\partial Y} + \frac{\partial \bar{\Psi}_y}{\partial X} \right) \right. \\ & \left. - \frac{8}{3h^2} E_{26}^* \frac{\partial^2 \bar{W}}{\partial X \partial Y} \right] - \frac{1}{2} \left(\frac{\partial \bar{W}}{\partial Y} \right)^2 - \frac{\partial \bar{W}}{\partial Y} \frac{\partial \bar{W}^*}{\partial Y} \\ & \left. - (A_{12}^* \bar{N}_x^T + A_{22}^* \bar{N}_y^T) \right\} \mathrm{d}Y \mathrm{d}X = 0. \end{aligned} \tag{8b}$$

Although the governing equations (1a)–(1d) have the same forms for the compressive buckling and tension buckling problems, unlike the compressive buckling problem [25,26], in the current study, the equilibrium of force in the X-direction is expressed as

$$\int_0^b \bar{N}_x \ \mathrm{d}Y - \sigma_x b h = 0, \tag{9}$$

where σ_x denotes the average tensile stress at $X = 0$ and $X = a$ edges.

In equation (8b), the reduced stiffness coefficients are contained in the reduced stiffness matrices, including $[A_{ij}^*]$, $[B_{ij}^*]$, $[D_{ij}^*]$, $[E_{ij}^*]$, $[F_{ij}^*]$, and $[H_{ij}^*]$. They can be obtained by [1]

$$\begin{aligned} \mathbf{A}^* &= \mathbf{A}^{-1}, \quad \mathbf{E}^* = -\mathbf{A}^{-1}\mathbf{E}, \\ \mathbf{B}^* &= -\mathbf{A}^{-1}\mathbf{B}, \quad \mathbf{F}^* = \mathbf{F} - \mathbf{E}\mathbf{A}^{-1}\mathbf{B}, \\ \mathbf{D}^* &= \mathbf{D} - \mathbf{B}\mathbf{A}^{-1}\mathbf{B}, \quad \mathbf{H}^* = \mathbf{H} - \mathbf{E}\mathbf{A}^{-1}\mathbf{E}, \end{aligned} \tag{10}$$

where the plate stiffness coefficients A_{ij}, B_{ij}, *etc.*, are expressed as

$$\begin{aligned} & (A_{ij}, B_{ij}, D_{ij}, E_{ij}, F_{ij}, H_{ij}) \\ & = \sum_{k=1}^{h_k} \int_{h_{k-1}} (\bar{Q}_{ij})_k (1, Z, Z^2, Z^3, Z^4, Z^6) \mathrm{d}Z, \ (i, j = 1, 2, 6), \end{aligned} \tag{11a}$$

$$(A_{ij}, D_{ij}, F_{ij}) = \sum_{k=1}^{h_k} \int_{h_{k-1}} (\bar{Q}_{ij})_k (1, Z^2, Z^4) \mathrm{d}Z, \ (i, j = 4, 5). \tag{11b}$$

3 Solution procedure

In order to solve the buckling and postbuckling problems of nanocomposite structures analytically, the Ritz and Galerkin methods are usually employed [31–38]. The accuracy of applying the Ritz and Galerkin methods depends strongly on the chosen modal shape functions. Shen [39] developed a two-step perturbation approach that gives explicit analytical expressions of all the variables in the large deflection region. The advantage of this method is that it is unnecessary to guess the form of the modal shape function, which can be obtained step by step, and such solutions satisfy both the governing equations and the boundary conditions accurately in the asymptotic sense. This approach has been applied to successfully solve various plate nonlinear boundary-value problems by other research teams [40–50]. To employ this approach for solving the postbuckling problem of auxetic laminated plates with in-plane NPR, the governing equations (1a)–(1d) are first converted into the non-dimensional forms as

$$\begin{aligned} & L_{11}(W) - L_{12}(\Psi_x) - L_{13}(\Psi_y) + \gamma_{14} L_{14}(F) - L_{16}(M^T) \\ & \quad + K_1 W - K_2 \nabla^2 W = \gamma_{14} \beta^2 L(W + W^*, F), \end{aligned} \tag{12a}$$

$$\begin{aligned} & L_{21}(F) + \gamma_{24} L_{22}(\Psi_x) + \gamma_{24} L_{23}(\Psi_y) - \gamma_{24} L_{24}(W) \\ & \quad = -\frac{1}{2} \gamma_{24} \beta^2 L(W + 2W^*, W), \end{aligned} \tag{12b}$$

$$L_{31}(W) + L_{32}(\Psi_x) - L_{33}(\Psi_y) + \gamma_{14} L_{34}(F) - L_{36}(S^T) = 0, \tag{12c}$$

$$L_{41}(W) - L_{42}(\Psi_x) + L_{43}(\Psi_y) + \gamma_{14} L_{44}(F) - L_{46}(S^T) = 0, \tag{12d}$$

where the non-dimensional operators $L_{ij}(\ )$ and $L(\ )$ are given in the study of Shen [1]. Note that the operators $L_{15}(\ )$, $L_{25}(\ )$, $L_{35}(\ )$, and $L_{45}(\ )$ vanish due to the uniform temperature field. The dimensionless parameters are defined by

$$x = \pi \frac{X}{a}, \ y = \pi \frac{Y}{b}, \ \beta = \frac{a}{b}, \ (W, W^*) = \frac{(\bar{W}, \bar{W}^*)}{[D_{11}^* D_{22}^* A_{11}^* A_{22}^*]^{1/4}},$$

$$F = \frac{\bar{F}}{[D_{11}^* D_{22}^*]^{1/2}}, \ (\Psi_x, \Psi_y) = \frac{a}{\pi} \frac{(\bar{\Psi}_x, \bar{\Psi}_y)}{[D_{11}^* D_{22}^* A_{11}^* A_{22}^*]^{1/4}},$$

$$\gamma_{14} = \left[\frac{D_{22}^*}{D_{11}^*} \right]^{1/2}, \ \gamma_{24} = \left[\frac{A_{11}^*}{A_{22}^*} \right]^{1/2},$$

$$\gamma_5 = -\frac{A_{12}^*}{A_{22}^*}, \ (\gamma_{T1}, \gamma_{T2}) = \frac{a^2}{\pi^2} \frac{(A_x^T, A_y^T)}{[D_{11}^* D_{22}^*]^{1/2}},$$

$$(K_1, k_1) = \bar{K}_1 \left(\frac{a^4}{\pi^4 D_{11}^*}, \ \frac{b^4}{E_0 h^3} \right), \ (K_2, k_2) = \bar{K}_2 \left(\frac{a^2}{\pi^2 D_{11}^*}, \ \frac{b^2}{E_0 h^3} \right),$$

$$(M_x,\ M_y,\ P_x,\ P_y) = \frac{a^2}{\pi^2}\frac{1}{D_{11}^*[D_{11}^*D_{22}^*A_{11}^*A_{22}^*]^{1/4}}\left(\bar{M}_x,\ \bar{M}_y,\ \frac{4}{3h^2}\bar{P}_x,\ \frac{4}{3h^2}\bar{P}_y\right),$$

$$(\lambda_x,\ \lambda_y) = \frac{(\sigma_x b^2 h,\ \sigma_y a^2 h)}{4\pi^2[D_{11}^*D_{22}^*]^{1/2}}, \tag{13}$$

where k_1 and k_2 are only utilized for numerical examples in Section 4, E_0 is the reference value of Young's modulus for the single-crystal copper matrix at T = 300 K, and is set to be E_0 = 101.14 GPa [22]. A_x^T, D_x^T, F_x^T, *etc.*, are given by

$$\begin{bmatrix} A_x^T & D_x^T & F_x^T \\ A_y^T & D_y^T & F_y^T \end{bmatrix} = -\sum_{k=1}^{h_k}\int_{h_{k-1}}\begin{bmatrix} A_x \\ A_y \end{bmatrix}_k (1, Z, Z^3)\mathrm{d}Z. \tag{14}$$

Accordingly, the plate boundary conditions on the x = 0 and $x = \pi$ edges can be nondimensionalized as

$$W = \Psi_y = 0,\ M_x = P_x = 0, \tag{15a}$$

and those on the y = 0 and $y = \pi$ edges can be nondimensionalized as

$$W = \Psi_x = 0,\ M_y = P_y = 0. \tag{15b}$$

And, hence, the in-plane boundary condition for the plate becomes

$$\int_0^\pi\int_0^\pi\left\{\left[\frac{\partial^2 F}{\partial x^2} - \gamma_5\beta^2\frac{\partial^2 F}{\partial y^2} + \gamma_{24}\gamma_{230}\left(\beta\frac{\partial \Psi_x}{\partial y} + \frac{\partial \Psi_y}{\partial x}\right)\right.\right.$$
$$\left.\left. -2\gamma_{24}\gamma_{526}\beta\frac{\partial^2 W}{\partial x\partial y}\right] - \frac{1}{2}\gamma_{24}\beta^2\left(\frac{\partial W}{\partial y}\right)^2 - \gamma_{24}\beta^2\frac{\partial W}{\partial y}\frac{\partial W^*}{\partial y}$$
$$+(\gamma_{T2} - \gamma_5\gamma_{T1})\Delta T\right\}\mathrm{d}y\mathrm{d}x = 0, \tag{16}$$

where γ_{230} and γ_{526} are defined in the study of Shen [1].

For the auxetic laminated plate subjected to uniaxial tension, equation (9) becomes

$$\frac{1}{\pi}\int_0^\pi \beta^2\frac{\partial^2 F}{\partial y^2}\mathrm{d}y - 4\lambda_x\beta^2 = 0. \tag{17}$$

The initial geometric imperfection of the auxetic laminated plate in the dimensionless form is given by

$$W^*(x, y, \varepsilon) = \varepsilon\mu A_{11}^{(1)}(\sin mx\ \sin ny), \tag{18}$$

where ε is the small perturbation parameter and μ is the imperfection parameter.

By employing the two-step perturbation approach, the asymptotic solutions of equations (12a)–(12d) along with the boundary conditions (15a) and (15b) are obtained as follows:

$$\begin{aligned} W = {} & \varepsilon[A_{11}^{(1)}\sin mx\ \sin ny] + \varepsilon^3[A_{13}^{(3)}\sin mx\ \sin 3ny \\ & + A_{31}^{(3)}\sin 3mx\ \sin ny] + \varepsilon^4[A_{22}^{(4)}\sin 2mx\ \sin 2ny \\ & + A_{24}^{(4)}\sin 2mx\ \sin 4ny + A_{42}^{(4)}\sin 4mx\ \sin 2ny] \\ & + O(\varepsilon^5), \end{aligned} \tag{19}$$

$$\begin{aligned} \Psi_x = {} & \varepsilon[C_{11}^{(1)}\cos mx\ \sin ny] + \varepsilon^2[C_{02}^{(2)}\sin 2ny] \\ & + \varepsilon^3[C_{13}^{(3)}\cos mx\ \sin 3ny + C_{31}^{(3)}\cos 3mx\ \sin ny] \\ & + \varepsilon^4[C_{02}^{(4)}\sin 2ny + C_{04}^{(4)}\sin 4ny \\ & + C_{22}^{(4)}\cos 2mx\ \sin 2ny + C_{24}^{(4)}\cos 2mx\ \sin 4ny \\ & + C_{42}^{(4)}\cos 4mx\ \sin 2ny] + O(\varepsilon^5), \end{aligned} \tag{20}$$

$$\begin{aligned} \Psi_y = {} & \varepsilon[D_{11}^{(1)}\sin mx\ \cos ny] + \varepsilon^2[D_{20}^{(2)}\sin 2mx] \\ & + \varepsilon^3[D_{13}^{(3)}\sin mx\ \cos 3ny + D_{31}^{(3)}\sin 3mx\ \cos ny] \\ & + \varepsilon^4[D_{20}^{(4)}\sin 2mx + D_{40}^{(4)}\sin 4mx \\ & + D_{22}^{(4)}\sin 2mx\ \cos 2ny + D_{24}^{(4)}\sin 2mx\ \cos 4ny \\ & + D_{42}^{(4)}\sin 4mx\ \cos 2ny] + O(\varepsilon^5). \end{aligned} \tag{21}$$

Note that to restrict the lateral expansion of the auxetic laminated plate subjected to uniaxial tensile loads, compressive stresses are produced in two unloaded edges that are immovable, so that

$$\begin{aligned} F = {} & -b_{00}^{(0)}\frac{x^2}{2} + B_{00}^{(0)}\frac{y^2}{2} + \varepsilon[B_{11}^{(1)}\cos\ mx\ \cos\ ny] \\ & + \varepsilon^2\left[-b_{00}^{(2)}\frac{x^2}{2} + B_{00}^{(2)}\frac{y^2}{2} + B_{20}^{(2)}\cos 2mx\right. \\ & \left. + B_{02}^{(2)}\cos 2ny\right] + \varepsilon^3\left[B_{13}^{(3)}\cos mx\ \cos 3ny\right. \\ & \left. + B_{31}^{(3)}\cos 3mx\ \cos ny\right] + \varepsilon^4\left[-b_{00}^{(4)}\frac{x^2}{2} + B_{00}^{(4)}\frac{y^2}{2}\right. \\ & + B_{20}^{(4)}\cos 2mx + B_{02}^{(4)}\cos 2ny \\ & + B_{22}^{(4)}\cos 2mx\ \cos 2ny + B_{40}^{(4)}\cos 4mx \\ & + B_{04}^{(4)}\cos 4ny + B_{24}^{(4)}\cos 2mx\ \cos 4ny \\ & \left. + B_{42}^{(4)}\cos 4mx\ \cos 2ny\right] + O(\varepsilon^5). \end{aligned} \tag{22}$$

It is worth noting that solution (22) is different from that obtained for the compressive postbuckling problem, as reported in the study of Shen *et al.* [25]. Thereafter, by substituting equation (22) into equation (17), one has

$$\lambda_x = \frac{1}{4\beta^2}(\beta^2 B_{00}^{(0)} + \varepsilon^2\beta^2 B_{00}^{(2)} + \varepsilon^4\beta^2 B_{00}^{(4)} + \cdots). \tag{23}$$

Similarly, we have

$$\lambda_y = (b_{00}^{(0)} + \varepsilon^2 b_{00}^{(2)} + \varepsilon^4 b_{00}^{(4)} + \cdots). \tag{24}$$

From perturbation procedure, we can obtain the expressions for $(-m^2\beta^2B_{00}^{(j)} + n^2\beta^2b_{00}^{(j)})$, ($j$ = 0, 2, 4,...) step by step, and adding them yields

$$\begin{aligned}&\gamma_{14}[-m^2(\beta^2B_{00}^{(0)} + \varepsilon^2\beta^2B_{00}^{(2)} + \varepsilon^4\beta^2B_{00}^{(4)} + \cdots) + n^2\beta^2(b_{00}^{(0)} \\ &+ \varepsilon^2b_{00}^{(2)} + \varepsilon^4b_{00}^{(4)} + \cdots)] \\ &\quad = \frac{Q_{11}}{(1+\mu)} + \frac{1}{16}\gamma_{14}\gamma_{24}\Theta_2(1+2\mu)(A_{11}^{(1)}\varepsilon)^2 \\ &\quad - \frac{1}{256}\gamma_{14}^2\gamma_{24}^2\Theta_{44}(1+\mu)(1+2\mu)(A_{11}^{(1)}\varepsilon)^4 + \cdots,\end{aligned} \tag{25}$$

and substituting W, Ψ_x, Ψ_y, and F into equation (16) yields

$$\begin{aligned}&-(b_{00}^{(0)} + \varepsilon^2b_{00}^{(2)} + \varepsilon^4b_{00}^{(4)} + \ldots) - \gamma_5(\beta^2B_{00}^{(0)} + \varepsilon^2\beta^2B_{00}^{(2)} \\ &\quad + \varepsilon^4\beta^2B_{00}^{(4)} + \cdots) \\ &-\frac{1}{8}\gamma_{24}n^2\beta^2(1+2\mu)(A_{11}^{(1)}\varepsilon)^2 + (\gamma_{T2} - \gamma_5\gamma_{T1})\Delta T = 0.\end{aligned} \tag{26}$$

From equations (25) and (26), we obtain

$$\begin{aligned}\lambda_y = \frac{\gamma_5}{\gamma_{14}(m^2 + \gamma_5 n^2\beta^2)}&\left[\frac{Q_{11}}{(1+\mu)} - S_0^T\right. \\ &+ \frac{1}{16}\gamma_{14}\gamma_{24}\left(\Theta_2 - \frac{2m^2n^2\beta^2}{\gamma_5}\right)(1+2\mu)(A_{11}^{(1)}\varepsilon)^2 \\ &\left. - \frac{1}{256}\gamma_{14}^2\gamma_{24}^2\Theta_{44}(1+\mu)(1+2\mu)(A_{11}^{(1)}\varepsilon)^4 + \cdots\right],\end{aligned} \tag{27}$$

where $(A_{11}^{(1)}\varepsilon)$ is treated as the second perturbation parameter and is related to the non-dimensional plate deflection W_m. From equation (19), one has

$$A_{11}^{(1)}\varepsilon = W_m + \Theta_3(W_m)^3\cdots. \tag{28}$$

In the current study, buckling is caused by compressed stress on the unloaded edges. By minimizing the compressive stress in equation (27) with respect to m and n, the buckling load of a perfect plate can readily be numerically obtained by setting μ = 0 (or $\bar{W}^*/h$ = 0), while taking W_m = 0 (or $\bar{W}/h$ = 0). The corresponding buckling mode (m, n) is obtained simultaneously, which determines the number of half-waves in the X and Y directions, respectively.

After the buckling mode (m, n) and buckling loads are determined, the postbuckling tensile load–deflection curve can be obtained as

$$\lambda_x = -\frac{1}{4\gamma_5\beta^2}\left[\lambda_y + \frac{1}{8}\gamma_{24}n^2\beta^2(1+2\mu)(A_{11}^{(1)}\varepsilon)^2 + \ldots\right]. \tag{29}$$

All symbols used in equations (27)–(29) are explained in Appendix.

4 Numerical results

In this section, we will present numerical studies for tension buckling and postbuckling behavior of perfect and imperfect auxetic nanocomposite laminated plates with in-plane NPR that are rested on elastic foundations. Two types of nanocomposite materials are selected for each ply of the laminated plate. One is the graphene/Cu composite with the graphene weight fraction w_G = 3%, while another is the CNT/Cu composite with the CNT weight fraction w_{CNT} = 3%. The material properties of the two composites are both temperature-dependent and are taken from the molecular dynamics simulation results of Fan *et al.* [21] and Zhang *et al.* [22], respectively, which are listed in Tables 1 and 2, respectively.

In the current research, symmetric $(0/90/0)_S$ and antisymmetric $(10/-10)_{3T}$ laminated rectangular plates are considered. The thickness of each ply is identical and the total thickness of the plate is h = 1.2 mm. The plate aspect ratios are selected as a/b = 2, 3, 4, and 5. To avoid cases where stresses increase beyond the elastic range, the plate width-to-thickness ratio is set as b/h = 50, 100, and 200. The in-plane effective Poisson's ratio (EPR) ν_{12}^e of these nanocomposite laminated plates are determined by employing the method as reported in the study of Shen *et al.* [51], and listed in Table 3. From Table 3, it can be seen that the absolute value of NPR of $(0/90/0)_S$ CNT/Cu laminated plate is the largest, whereas that of the $(10/-10)_{3T}$ graphene/Cu laminated plate is the smallest at all three temperature levels considered.

The buckling load is of practical concern of the nanocomposite laminated plates and, therefore, we need to determine the buckling tensile load and the corresponding buckling mode for the auxetic nanocomposite laminated

Table 1: Temperature-dependent properties of graphene/Cu composites (w_G = 3%) [21]

	T = 300 K	T = 500 K	T = 700 K
E_{11} (GPa)	207.55	193.15	180.50
E_{22} (GPa)	196.69	183.94	171.58
E_{33} (GPa)	61.454	55.773	47.192
G_{12} (GPa)	66.389	62.092	58.314
G_{13} (GPa)	33.617	31.536	28.928
G_{23} (GPa)	32.327	31.009	28.200
ν_{12}	−0.0649	−0.0721	−0.0751
ν_{13}	0.6297	0.6298	0.6826
ν_{23}	0.6512	0.6617	0.6742
α_{11} (×10^{-6} K^{-1})	1.4224	1.5037	1.6222
α_{22} (×10^{-6} K^{-1})	1.4194	1.5006	1.6278

Table 2: Temperature-dependent properties of CNT/Cu composites (w_{CNT} = 3%) [22]

	T = 300 K	T = 500 K	T = 700 K
E_{11} (GPa)	226.24	216.70	209.84
E_{22} (GPa)	96.918	89.186	81.311
E_{33} (GPa)	68.336	63.629	59.185
G_{12} (GPa)	15.496	14.090	12.584
G_{13} (GPa)	48.932	45.508	42.145
G_{23} (GPa)	49.838	46.357	43.688
ν_{12}	−0.1537	−0.1637	−0.1762
ν_{13}	0.7508	0.7677	0.7833
ν_{23}	0.8121	0.8215	0.8316
α_{11} (×10^{-6} K^{-1})	8.3366	8.3227	8.3089
α_{22} (×10^{-6} K^{-1})	12.649	13.000	13.349

plates first. Since the tension buckling of the auxetic laminated plates is investigated for the first time, no experimental data are currently available for model validation. In order to validate the accuracy and reliability of the present solution method, the finite element analysis is performed and the results are depicted in Figure 2. The buckling load associated with the buckling mode agrees well in each case, which clearly shows the validity and accuracy of the current solution for the tension buckling analysis of auxetic laminated plates.

Buckling tensile loads P_{cr} (kN) of the $(0/90/0)_S$ and $(10/-10)_{3T}$ graphene/Cu laminated plates and $(0/90/0)_S$ CNT/Cu laminated plates, with different values of plate aspect ratios (a/b = 2, 3, and 4) rested on the elastic foundations under temperature conditions are presented in Tables 4–6. The thermal environments are set as T = 300, 500, and 700 K. Two foundation models with (k_1, k_2) = (10, 0) for the Winkler foundation and (k_1, k_2) = (10, 1) for the Pasternak foundation are considered. Owing to the NPR effect, the applied tensile load acting in the longitudinal direction produces a compressive reaction force and, hence, compressive stress, when the transverse displacement is constrained. Buckling occurs when the compressive stress reaches a critical value. As can be observed, the buckling tensile loads for the $(10/-10)_{3T}$ graphene/Cu laminated plates are larger than those of the $(0/90/0)_S$ graphene/Cu laminated plates, whereas the buckling tensile loads of the $(0/90/0)_S$ CNT/Cu laminated plates are lower than those of the $(0/90/0)_S$ graphene/Cu laminated plates, even if the $(0/90/0)_S$ CNT/Cu laminated plate is relatively thicker (*i.e.*, lower b/h) than the $(0/90/0)_S$ graphene/Cu laminated plate. This is because the $(10/-10)_{3T}$ graphene/Cu laminated plate has the lowest

Table 3: Effective Poisson's ratios ν_{12}^e for nanocomposite laminates

T (K)	CNT/Cu laminates	Graphene/Cu laminates	
	$(0/90/0)_S$	$(0/90/0)_S$	$(10/-10)_{3T}$
300	−0.111	−0.064	−0.040
500	−0.115	−0.071	−0.047
700	−0.120	−0.074	−0.050

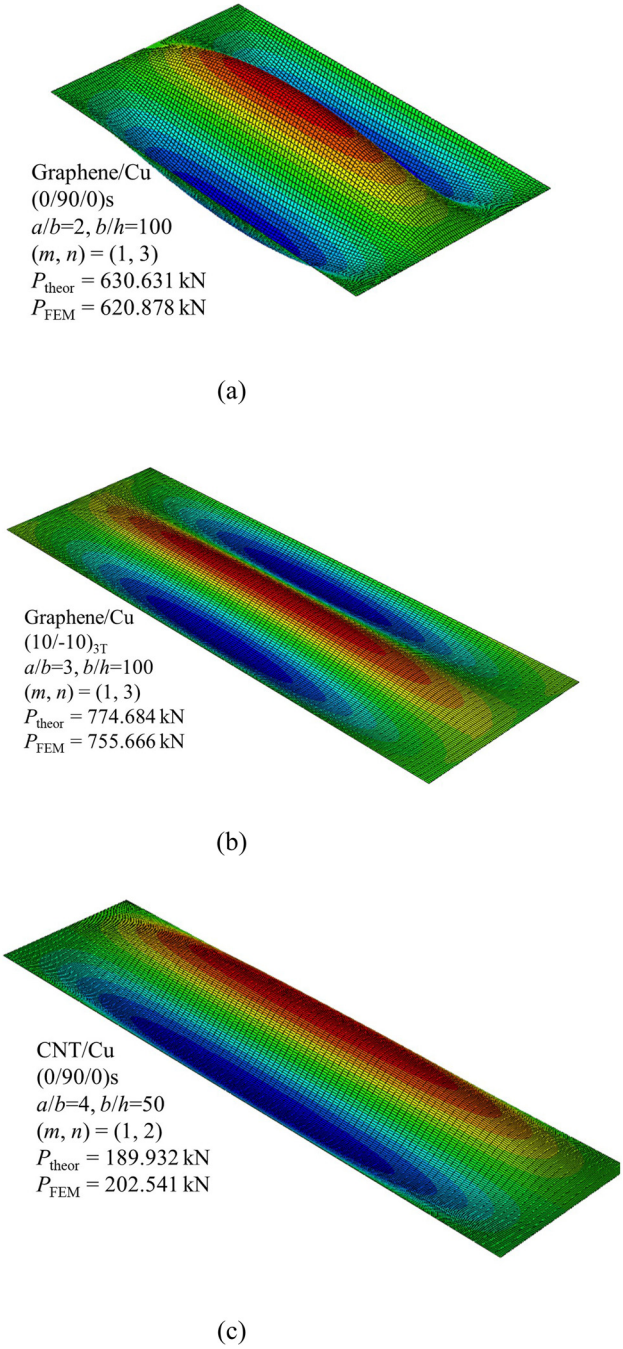

Figure 2: Comparisons of buckling loads of nanocomposite laminated plates under uniaxial tension: (a) a/b = 2, (m, n) = (1,3); (b) a/b = 3, (m, n) = (1,3); and (c) a/b = 4, (m, n) = (1,2).

Table 4: Buckling tensile loads P_{cr} (kN) of $(0/90/0)_S$ laminated plates made of graphene/Cu with unloaded edges that are immovable [h = 1.2 mm, b/h = 100]

T (K)	a/b = 2	a/b = 3	a/b = 4
(k_1, k_2) = (0, 0)			
300	630.6308 (1, 3)[a]	281.1347 (1, 2)	205.3563 (1, 2)
500	199.6882 (1, 2)	209.9876 (1, 3)	189.8835 (1, 3)
700	62.7413 (1, 3)	40.8513 (1, 3)	35.6539 (1, 3)
(k_1, k_2) = (10, 0)			
300	635.3398 (1, 3)	291.7302 (1, 2)	213.2104 (1, 2)
500	250.4258 (1, 2)	212.8428 (1, 3)	192.4932 (1, 3)
700	66.4007 (1, 3)	43.5732 (1, 3)	38.1518 (1, 6)
(k_1, k_2) = (10, 1)			
300	678.3310 (1, 3)	334.7214 (1, 2)	244.7016 (1, 2)
500	335.6300 (1, 3)	238.5179 (1, 3)	215.8357 (1, 3)
700	99.8081 (1, 3)	68.0491 (1, 3)	60.4938 (1, 3)

[a]Buckling mode (m, n).

Table 6: Buckling tensile loads P_{cr} (kN) of $(0/90/0)_S$ laminated plates made of CNT/Cu with unloaded edges that are immovable [h = 1.2 mm, b/h = 50]

T (K)	a/b = 2	a/b = 3	a/b = 4
(k_1, k_2) = (0, 0)			
300	523.3330 (1, 3)[a]	233.8883 (1, 2)	189.9320 (1, 2)
500	118.3289 (1, 3)	91.2130 (1, 3)	84.3524 (1, 3)
700	86.4904 (1, 4)	75.9266 (1, 4)	72.7877 (1, 4)
(k_1, k_2) = (10, 0)			
300	529.4551 (1, 3)	247.6630 (1, 2)	201.1594 (1, 2)
500	176.8505 (1, 3)	95.8015 (1, 3)	88.6184 (1, 3)
700	89.1192 (1, 4)	78.2660 (1, 4)	75.0403 (1, 4)
(k_1, k_2) = (10, 1)			
300	585.3463 (1, 3)	303.5543 (1, 2)	246.1761 (1, 2)
500	230.2771 (1, 3)	137.0625 (1, 3)	126.7755 (1, 3)
700	131.2807 (1, 4)	115.4652 (1, 4)	110.7512 (1, 4)

[a]Buckling mode (m, n).

negative EPR, while the $(0/90/0)_S$ CNT/Cu laminated plate has the highest negative EPR among the three. In other words, a higher negative EPR will exacerbate the compressive stress caused by the reaction force, and hence, make the composites more prone to buckle. We also observe that the buckling mode (m, n) changes from (1, 3) to (1, 2) for the $(0/90/0)_S$ CNT/Cu and graphene/Cu laminated plates, whereas the buckling mode (m, n) changes from (1, 4) to (1, 2) for the $(10/-10)_{3T}$ graphene/Cu laminated plates when the plate aspect ratio a/b changes from 2 to 4. The changes in the buckling mode can also be observed when the temperature increases from 300 to 700 K. These simulation results indicate that changing the aspect ratio of the plates and applying the temperature condition significantly affect the distribution of the compressive stress along the unloaded edges, thereby resulting in shifts in the buckling mode. Additionally, similar to cases of compressive buckling [25], the buckling tensile loads decrease when the temperature increases and increase when the foundation stiffnesses are increased.

Table 5: Buckling tensile loads P_{cr} (kN) of $(\pm10)_{3T}$ laminated plates made of graphene/Cu with unloaded edges that are immovable [h = 1.2 mm, b/h = 100]

T (K)	a/b = 2	a/b = 3	a/b = 4
(k_1, k_2) = (0, 0)			
300	1569.6150 (1, 4)[a]	774.6838 (1, 3)	395.1861 (1, 2)
500	658.9609 (1, 3)	345.4806 (1, 3)	294.1510 (1, 3)
700	131.6798 (1, 3)	65.4747 (1, 3)	53.8327 (1, 3)
(k_1, k_2) = (10, 0)			
300	1573.5280 (1, 4)	780.7916 (1, 3)	410.8407 (1, 2)
500	667.8953 (1, 3)	350.3338 (1, 3)	298.3353 (1, 3)
700	139.4096 (1, 3)	69.9492 (1, 3)	57.7324 (1, 3)
(k_1, k_2) = (10, 1)			
300	1636.2960 (1, 4)	835.7136 (1, 3)	473.6080 (1, 2)
500	749.4606 (1, 3)	393.9758 (1, 3)	335.7609 (1, 3)
700	209.9779 (1, 3)	110.1851 (1, 3)	92.6123 (1, 3)

[a]Buckling mode (m, n).

Figure 3 shows the effect of plate aspect ratio a/b (= 3, 4 and 5) on the postbuckling behavior of $(0/90/0)_S$ and $(\pm10)_{3T}$ graphene/Cu and $(0/90/0)_S$ CNT/Cu laminated plates under tension at T = 300 K. The depicted curves in Figure 3 indicate that increasing the plate aspect ratio significantly reduces the critical tension buckling load as well as the peak of the postbuckling load–deflection curves. These simulation results suggest that in the postbuckling range, the increase of the amplitude of the plate deflection will counteract the lateral expansion displacement of the auxetic plate. The stress on the unloaded edges changes from compressive stress to tensile stress when the amplitude of the plate deflection reaches a certain value, which leads the tensile load–deflection curve to switch from rising to falling at the peak point. The postbuckling curves of tensile load *vs* deflection for the imperfect auxetic laminated plates are also plotted in Figure 3, where $\bar{W}^*/h$ = 0.1 (or 0.05) denotes the non-dimensional maximum initial geometric imperfection of the auxetic laminated plates.

The effect of plate width-to-thickness ratio on the postbuckling behavior of the three configurations of auxetic laminated plates with a/b = 3 under tension at 300 K is illustrated in Figure 4. Three cases of b/h = 50, 100, and 200 are chosen for the $(0/90/0)_S$ CNT/Cu and graphene/Cu laminated plates, while b/h is set as 100, 150, and 200 for the $(10/-10)_{3T}$ graphene/Cu laminated plates. Such choices of the b/h ratios for the two types of laminates have ensured that the compressive or tensile stresses stay within the

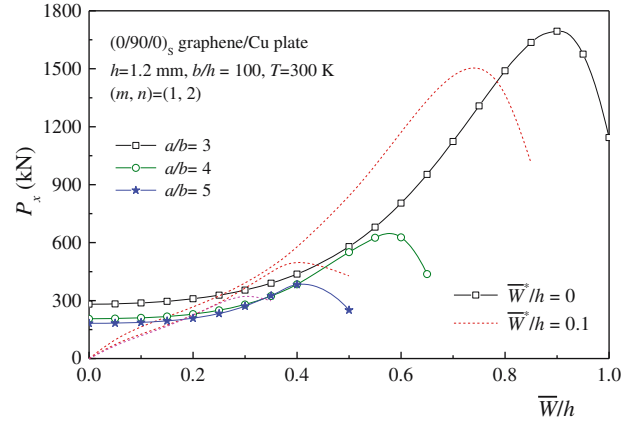

(a)

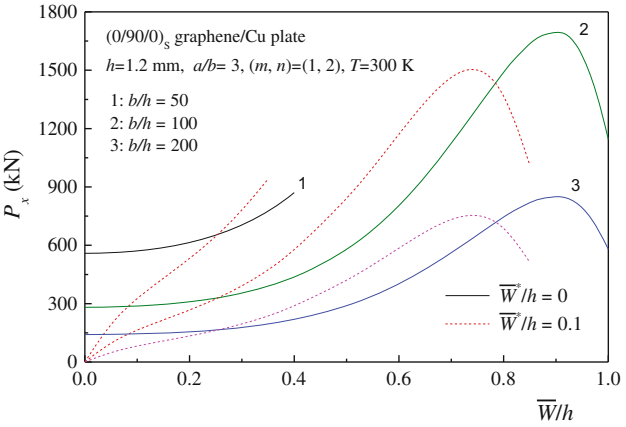

(a)

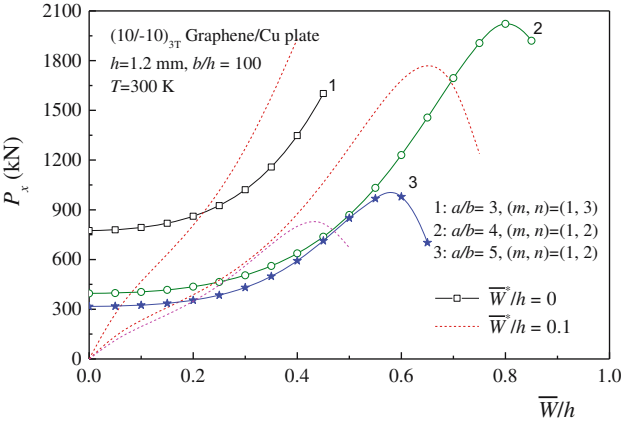

(b)

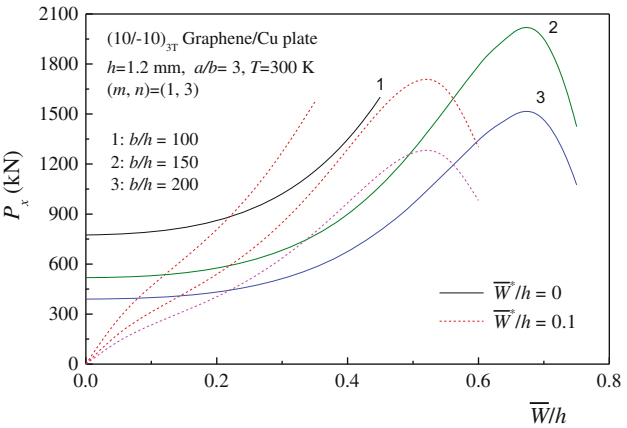

(b)

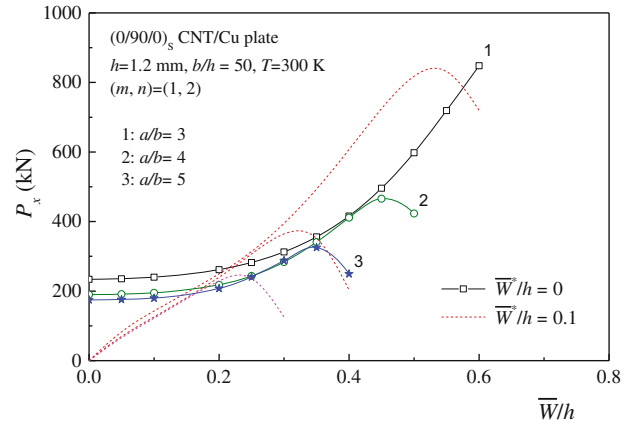

(c)

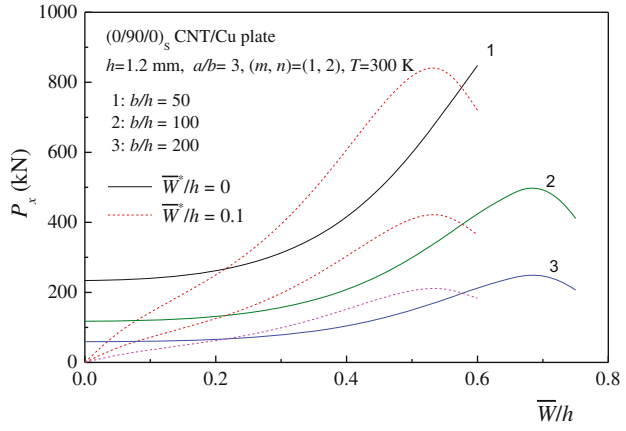

(c)

Figure 3: Effect of the plate aspect ratio on the postbuckling behavior of auxetic laminated plates under tension: (a) $(0/90/0)_S$ graphene/Cu plate; (b) $(10/-10)_{3T}$ graphene/Cu plate; and (c) $(0/90/0)_S$ CNT/Cu plate.

Figure 4: Effect of the plate width-to-thickness ratio on the postbuckling behavior of auxetic laminated plates under tension: (a) $(0/90/0)_S$ graphene/Cu plate; (b) $(10/-10)_{3T}$ graphene/Cu plate; and (c) $(0/90/0)_S$ CNT/Cu plate.

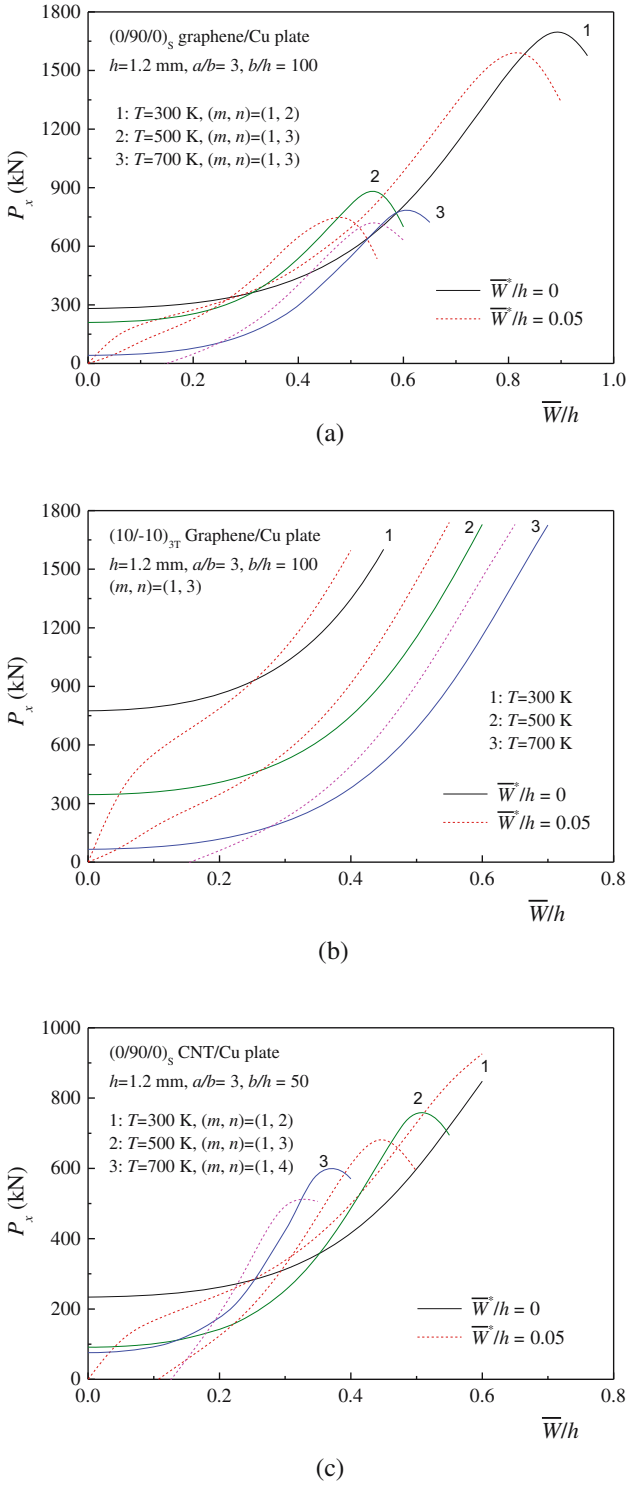

Figure 5: Effect of temperature variation on the postbuckling behavior of auxetic laminated plates under tension: (a) $(0/90/0)_S$ graphene/Cu plate; (b) $(10/-10)_{3T}$ graphene/Cu plate; and (c) $(0/90/0)_S$ CNT/Cu plate.

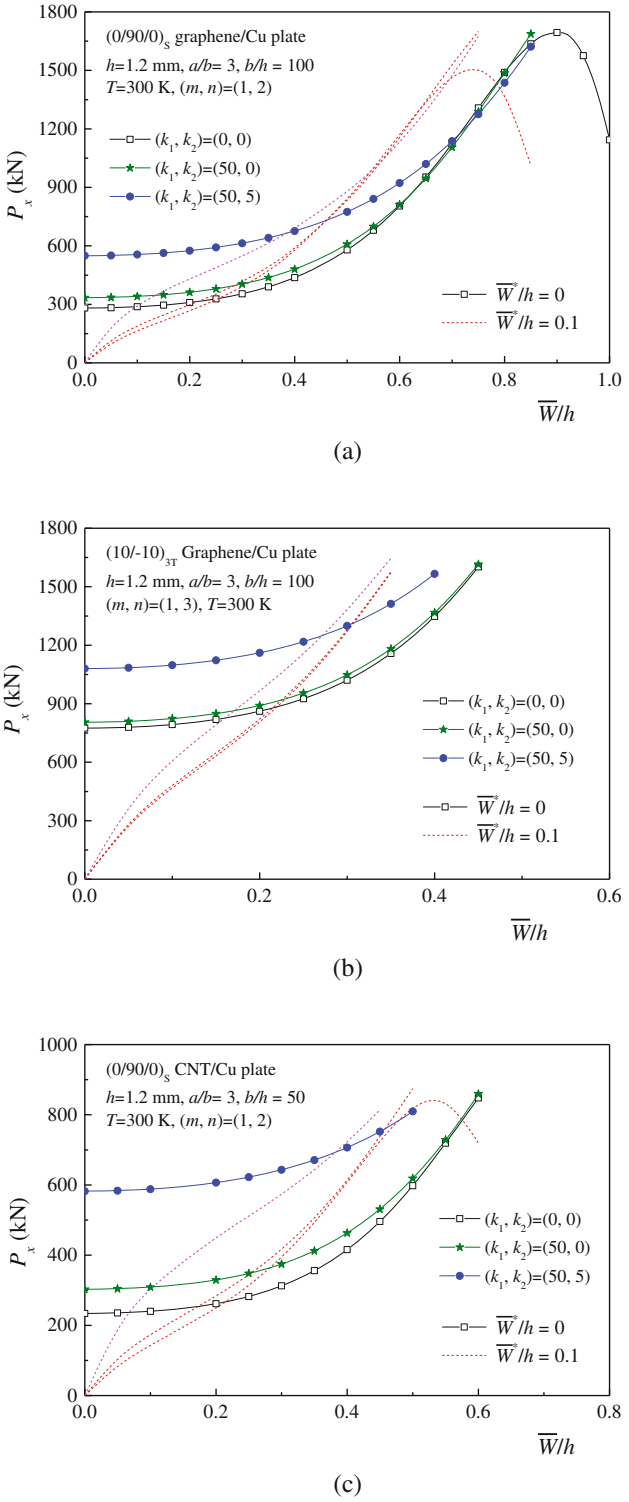

Figure 6: Effect of substrate stiffnesses on the postbuckling behavior of auxetic laminated plates under tension: (a) $(0/90/0)_S$ graphene/Cu plate; (b) $(10/-10)_{3T}$ graphene/Cu plate; and (c) $(0/90/0)_S$ CNT/Cu plate.

elastic range. As a result, no peak can be observed on the postbuckling tensile load–deflection curves for b/h = 50 for the $(0/90/0)_S$ laminated plates and b/h = 100 for the $(10/-10)_{3T}$ laminated plates. It is found that the postbuckling tensile load–deflection curves are reduced when the plate becomes thinner.

The effect of temperature change on the postbuckling behavior of three configurations of auxetic laminated plates with a/b = 3 is depicted in Figure 5. Three thermal environmental conditions, T = 300, 500, and 700 K, are considered. The temperature effect is included in the simulations by using the temperature-dependent material properties of both graphene/Cu and CNT/Cu composites. As the temperature increases, the elastic moduli reduce and the strength degrades for nanocomposites. As a result, the postbuckling tensile load–deflection curves are decreased as the temperature increases. Note that the initial geometric imperfection is set as $\bar{W}^*/h$ = 0.05 in this example. Our results show that the $(10/-10)_{3T}$ graphene/Cu laminated plate has no buckling mode change. Additionally, the postbuckling tensile load–deflection curve becomes extremely low at T = 700 K compared to the case at T = 300 K.

Figure 6 illustrates the effect of foundation stiffnesses on the postbuckling behavior of three configurations of auxetic laminated plates with a/b = 3 rested on elastic foundations at T = 300 K. In this example, two foundation models with (k_1, k_2) = (50, 0) for the Winkler foundation and (k_1, k_2) = (50, 5) for the Pasternak foundation are considered. Similar to conventional observations in laminated plates [25], the postbuckling curves of tensile load *vs* deflection increase with higher foundation stiffnesses. This implies that the tensile buckling could be mitigated by using a stiffer foundation as a substrate. Furthermore, no change in the buckling mode is observed when the auxetic laminated plate is supported by either the Winkler foundation or the Pasternak foundation.

5 Conclusion

Tension buckling and postbuckling phenomena of auxetic nanocomposite laminated plates with immovable unloaded edges are presented. The material properties of the two nanocomposites considered in this study, CNT/Cu and graphene/Cu composites, are both dependent on temperature. Based on the two-step perturbation method, the explicit analytical solutions are obtained for the first time. The numerical studies have been presented for three configurations of laminated plates, including $(0/90/0)_S$ and $(10/-10)_{3T}$ graphene/Cu laminated plates and $(0/90/0)_S$ CNT/Cu laminated plates, with or without an elastic substrate under temperature environments. The buckling tensile loads and associated buckling modes have been verified by FE simulation. The results presented explore for the first time the important issue of auxetic nanocomposite laminated plates, and thus are greatly useful in the engineering design of the novel nanocomposite structures. The findings are summarized as follows:

1) Due to the impact of in-plane NPR, the buckling tensile loads exist for the auxetic laminated rectangular plates with unloaded edges that are “immovable” under uniaxial tension. The tensile loads on “movable” ends lead to compressive stress on “immovable” ends, which is exactly the origin of tension buckling and postbuckling.
2) Unlike the traditional compressive postbuckling case where the postbuckling load–deflection curve rises slowly, in the tension postbuckling case, the postbuckling tensile load–deflection curve rises rapidly, in particular for cases when the temperature variation is under consideration.
3) In the postbuckling range, the increase of the amplitude of the plate deflection will counteract the lateral expansion displacement of the auxetic plate. The stress on the unloaded edges may shift from compressive stress to tensile stress when the amplitude of the plate deflection reaches a certain value. In most cases, a peak point exists on the postbuckling tensile load–deflection curves.

Funding information: Y. Fan would like to acknowledge financial support from the National Natural Science Foundation of China (NSFC) under Grant No. 12102255. Y. Wang would like to acknowledge financial support provided by the National Science Foundation under Award No. CMMI-2202737.

Author contributions: All authors have accepted responsibility for the entire content of this manuscript and approved its submission.

Conflict of interest: The authors state no conflict of interest.

References

[1] Shen H-S. Postbuckling Behavior of Plates and Shells. Singapore: World Scientific Publishing Co. Pte. Ltd; 2017.
[2] Shimizu S, Yoshida S, Enomoto N. Buckling of plates with a hole under tension. Thin-Walled Struct. 1991;12:35–49.
[3] Shimizu S. Tension buckling of plate having a hole. Thin-Walled Struct. 2007;45:827–33.
[4] Kremer T, Schurmann H. Buckling of tension-loaded thin-walled composite plates with cut-outs. Compos Sci Technol. 2008;68:90–7.
[5] Fujimoto T, Sumi S. Postbuckling behavior of centrally cracked plates under tension. JSME Int J. 1987;30:1714–23.
[6] Shaw D, Huang YH. Buckling behavior of a central cracked thin plate under tension. Eng Fract Mech. 1990;35:1019–27.
[7] Biks E, Bankin CC, Brogan FA. The buckling behavior of a central crack in a plate under tension. Eng Fract Mech. 1992;43:529–48.

[8] Segedin RH, Collins IF, Segedin CM. The elastic wrinkling of rectangular sheets. Int J Mech Sci. 1988;30:719–32.
[9] Cerda E, Ravi-Chandar K, Mahadevan L. Wrinkling of an elastic sheet under tension. Nature. 2002;419:579–80.
[10] Nayyar V, Ravi-Chandar K, Huang R. Stretch-induced stress patterns and wrinkles in hyperelastic thin sheets. Int J Solids Struct. 2011;48:3471–83.
[11] Puntel E, Deseri L, Fried E. Wrinkling of a stretched thin sheet. J Elast. 2011;105:137–70.
[12] Silvestre N. Wrinkling of stretched thin sheets: Is restrained Poisson's effect the sole cause? Eng Struct. 2016;106:195–208.
[13] Shen H-S, Xu Y-M, Zhang C-L. Graphene: why buckling occurs? Appl Phys Lett. 2013;102:131905.
[14] Xiang Y, Shen H-S. Tension buckling of graphene: a new phenotype. Solid State Commun. 2014;192:20–3.
[15] Wang C, Lan L, Tan H. The physics of wrinkling in graphene membranes under local tension. Phys Chem Chem Phys. 2013;15:2764–73.
[16] Huang J, Han Q. Wrinkling in graphene subjected to gradient tension. Nano. 2015;10:53–61.
[17] Dahiya M, Bansal SA. Graphene-reinforced nanocomposites: synthesis, micromechanics models, analysis and applications – a review. Proc IMechE Part C-J Mech Eng Sci. 2022;236:9218–40.
[18] Soni SK, Thomas B, Kar VR. A comprehensive review on CNTs and CNT-reinforced composites: syntheses, characteristics and applications. Mater Today Commun. 2020;25:101546.
[19] Fan Y, Xiang Y, Shen H-S. Temperature-dependent negative Poisson's ratio of monolayer graphene: Prediction from molecular dynamics simulations. Nanotechnol Rev. 2019;8:415–21.
[20] Zhang H-N, Fan Y, Shen H-S. Chirality-dependent and intrinsic auxeticity for single-walled carbon nanotubes. Materials. 2022;15:8720.
[21] Fan Y, Xiang Y, Shen H-S. Temperature-dependent mechanical properties of graphene/Cu nanocomposites with in-plane negative Poisson's ratios. Research. 2020;2020:5618021.
[22] Zhang H-N, Fan Y, Shen H-S. Prediction of temperature-dependent mechanical properties for SWCNT/Cu nanocomposite metamaterials: A molecular dynamics study. Nanomaterials. 2023;13:1885.
[23] Ren X, Das R, Tran P, Ngo TD, Xie YM. Auxetic metamaterials and structures: a review. Smart Mater Struct. 2018;27:023001.
[24] Fan Y, Wang Y. The effect of negative Poisson's ratio on the low-velocity impact response of an auxetic nanocomposite laminate beam. Int J Mech Mater Des. 2021;17:153–69.
[25] Shen H-S, Xiang Y, Reddy JN. Effect of negative Poisson's ratio on the post-buckling behavior of FG-GRMMC laminated plates in thermal environments. Compos Struct. 2020;253:112731.
[26] Chen XH, Shen H-S, Huang X-H. Thermo-mechanical postbuckling analysis of sandwich plates with functionally graded auxetic GRMMC core on elastic foundations. Compos Struct. 2022;279:114796.
[27] Librescu L, Stein M. A geometrically nonlinear theory of transversely isotropic laminated composite plates and its use in the postbuckling analysis. Thin-Walled Struct. 1991;11:177–201.
[28] Shen H-S, Xiang Y, Lin F, Hui D. Buckling and postbuckling of functionally graded graphene-reinforced composite laminated plates in thermal environments. Compos Part B-Eng. 2017;119:67–78.
[29] Shen H-S, Zhu ZH. Buckling and postbuckling behavior of functionally graded nanotube-reinforced composite plates in thermal environments. CMC-Comput Mater Continua. 2010;18:155–82.
[30] Reddy JN. A refined nonlinear theory of plates with transverse shear deformation. Int J Solids Struct. 1984;20:881–96.
[31] Sofiyev AH, Tornabene F, Dimitri R, Kuruoglu N. Buckling behavior of FG-CNT reinforced composite conical shells subjected to a combined loading. Nanomaterials. 2020;10:419.
[32] Sofiyev AH, Fantuzzi N. Stability analysis of shear deformable inhomogeneous nanocomposite cylindrical shells under hydrostatic pressure in thermal environment. Materials. 2023;16:4887.
[33] Mirzaei M, Kiani Y. Thermal buckling of temperature dependent FG-CNT reinforced composite plates. Meccanica. 2016;51:2185–201.
[34] Kiani Y. Thermal post-buckling of FG-CNT reinforced composite plates. Compos Struct. 2017;159:299–306.
[35] Kiani Y. Shear buckling of FG-CNT reinforced composite plates using Chebyshev-Ritz method. Compos Part B-Eng. 2016;105:176–87.
[36] Zeverdejani MK, Beni YT, Kiani Y. Multi-scale buckling and post-buckling analysis of functionally graded laminated composite plates reinforced by defective graphene sheets. Int J Struct Stab Dyn. 2020;20:2050001.
[37] Abbaspour F, Arvin H, Kiani Y. Mechanical buckling analysis of functionally graded composite laminated plates reinforced with temperature dependent graphene sheets resting on elastic foundation. ZAMM. 2022;102:e202100097.
[38] Guo H, Zur KK, Ouyang X. New insights into the nonlinear stability of nanocomposite cylindrical panels under aero-thermal loads. Compos Struct. 2023;303:116231.
[39] Shen H-S. A two-step perturbation method in nonlinear analysis of beams. Plates and Shells. Singapore: John Wiley & Sons Inc; 2013.
[40] Li ZM. Thermal postbuckling behavior of 3D braided rectangular plates. J Therm Stresses. 2011;34:626–49.
[41] Wang Z-X, Xu J, Qiao P. Nonlinear low-velocity impact analysis of temperature-dependent nanotube-reinforced composite plates. Compos Struct. 2014;108:423–34.
[42] Fu Y, Zhong J, Shao X, Tao C. Analysis of nonlinear dynamic stability for carbon nanotube-reinforced composite plates resting on elastic foundations. Mech Adv Mater Struct. 2016;23:1284–9.
[43] Fallah F, Nosier A, Sharifi M, Ghezelbash F. On perturbation method in mechanical, thermal and thermo-mechanical loadings of plates: cylindrical bending of FG plates. ZAMM. 2016;96:217–32.
[44] Najafi F, Shojaeefard MH, Googarchin HS. Nonlinear low-velocity impact response of functionally graded plate with nonlinear three-parameter elastic foundation in thermal field. Compos Part B-Eng. 2016;107:123–40.
[45] Fan Y, Wang H. Thermal postbuckling and vibration of postbuckled matrix cracked hybrid laminated plates containing carbon nanotube reinforced composite layers on elastic foundation. Compos Struct. 2016;157:386–97.
[46] Fan Y, Wang H. Nonlinear dynamics of matrix-cracked hybrid laminated plates containing carbon nanotube-reinforced composite layers resting on elastic foundations. Nonlinear Dyn. 2016;84:1181–99.
[47] Fan Y, Wang H. Nonlinear low-velocity impact analysis of matrix cracked hybrid laminated plates containing CNTRC layers resting on visco-Pasternak foundation. Compos Part B-Eng. 2017;117:9–19.
[48] Huang X-H, Yang J, Azim I, Ren X, Wang X. Static and dynamic analyses of auxetic hybrid FRC/CNTRC laminated plates. Nanotechnol Rev. 2020;9:1625–42.
[49] Huang X-H, Yang J, Wang X, Azim I. Combined analytical and numerical approach for auxetic FG-CNTRC plate subjected to a sudden load. Eng Comput. 2022;38:S55–70.
[50] Huang X-H, Yu N-T, Azim I, Zhu J, Wu M-J. A comparative analysis of thermos-mechanical behavior of CNT-reinforced composite plates: Capturing the effects of thermal shrinkage. Case Stud Therm Eng. 2022;38:102347.
[51] Shen H-S, Li C, Huang X-H. Assessment of negative Poisson's ratio effect on the postbuckling of pressure-loaded FG-CNTRC laminated cylindrical shells. Mech Based Des Struct Mach. 2023;51:1856–80.

Appendix

In equations (27) and (29),

$$S_0^T = \gamma_{14} n^2\beta^2(\gamma_{T2} - \gamma_5\gamma_{T1})\Delta T,$$

$$Q_{11} = \Theta_{11} + K_1 + K_2(m^2 + n^2\beta^2),\ \Theta_{22} = \left(\frac{m^4}{\gamma_7} + \frac{n^4\beta^4}{\gamma_6}\right),$$

$$\Theta_3 = \frac{1}{16}\gamma_{14}\gamma_{24}(m^2 + \gamma_5 n^2\beta^2)\left(\frac{m^4}{J_{13}\gamma_7} + \frac{n^4\beta^4}{J_{31}\gamma_6}\right)(1+\mu)^2(1+2\mu),$$

$$\Theta_{44} = (m^2 + \gamma_5 n^2\beta^2)\left(\frac{m^8}{J_{13}} + \frac{\gamma_{24}^4 n^8\beta^8}{J_{31}}\right)[2(1+\mu)^2 + (1+2\mu)], \quad \text{(A1)}$$

where (with other symbols being defined as in the study of Shen [1])

$$J_{13} = Q_{13}C_{11}(1+\mu) - Q_{11}C_{13} - J_{13}^T,$$
$$J_{31} = Q_{31}C_{11}(1+\mu) - Q_{11}C_{31} - J_{31}^T,$$
$$C_{11} = m^2 + \gamma_5 n^2\beta^2,$$
$$C_{13} = m^2 + 9\gamma_5 n^2\beta^2,\ C_{31} = 9m^2 + \gamma_5 n^2\beta^2,$$

$$Q_{13} = \Theta_{13} + [K_1 + K_2(m^2 + 9n^2\beta^2)],$$
$$Q_{31} = \Theta_{31} + [K_1 + K_2(9m^2 + n^2\beta^2)],$$

$$J_{31}^T = -J_{13}^T = 8\gamma_{14} m^2 n^2\beta^2(1+\mu)(\gamma_{T2} - \gamma_5\gamma_{T1})\Delta T,$$

$$\Theta_{11} = (m^4 + 2\gamma_{12} m^2 n^2\beta^2 + \gamma_{14}^2 n^4\beta^4) + \gamma_{14}\gamma_{24}\frac{m^2 n^2\beta^2(\gamma_{141}m^2 + \gamma_{143}n^2\beta^2)^2}{m^4 + 2\gamma_{22}m^2n^2\beta^2 + \gamma_{24}^2 n^4\beta^4},$$

$$\Theta_{13} = (m^4 + 18\gamma_{12} m^2 n^2\beta^2 + 81\gamma_{14}^2 n^4\beta^4) + \gamma_{14}\gamma_{24}\frac{9m^2 n^2\beta^2(\gamma_{141}m^2 + 9\gamma_{143}n^2\beta^2)^2}{m^4 + 18\gamma_{22}m^2n^2\beta^2 + 81\gamma_{24}^2 n^4\beta^4},$$

$$\Theta_{31} = (81m^4 + 18\gamma_{12} m^2 n^2\beta^2 + \gamma_{14}^2 n^4\beta^4) + \gamma_{14}\gamma_{24}\frac{9m^2 n^2\beta^2(9\gamma_{141}m^2 + \gamma_{143}n^2\beta^2)^2}{81m^4 + 18\gamma_{22}m^2n^2\beta^2 + \gamma_{24}^2 n^4\beta^4},$$

$$\gamma_6 = 1 + \gamma_{14}\gamma_{24}\gamma_{230}^2\frac{4m^2}{\gamma_{42} + \gamma_{322}4m^2},$$
$$\gamma_7 = \gamma_{24}^2 + \gamma_{14}\gamma_{24}\gamma_{223}^2\frac{4n^2\beta^2}{\gamma_{31} + \gamma_{322}4n^2\beta^2}. \quad \text{(A2)}$$